Hydrodynamic relaxations in the original dissipative particle dynamics model

J. S. Hansen*

"Glass and Time", IMFUFA, Department of Science and Environment, Roskilde University, Postbox 260, DK-4000 Roskilde, Denmark

Michael L. Greenfield

Department of Chemical Engineering, University of Rhode Island, Kingston, Rhode Island 02881, United States

Jeppe C. Dyre

"Glass and Time", IMFUFA , Department of Science and Environment, Roskilde University, Postbox 260, DK-4000 Roskilde, Denmark

Abstract

In this paper we study relaxation phenomena in the original dissipative particle dynamics (o-DPD) model. Using fluctuating hydrodynamics as the framework of the investigation, we focus on the collective transverse and longitudinal dynamics. It is shown that classical hydrodynamic theory predicts the transverse dynamics at relative low temperatures very well when compared to simulation data; the theory fails for high temperatures, however. This is consistent with the fact that for high temperatures the o-DPD model has gas-like behavior for which classical hydrodynamics is not applicable. The relaxation time for the transverse dynamics is consistent with the viscosity derived from stress correlations that include conservative forces, but neglect random and dissipative contributions. For high temperatures, the spectrum for the longitudinal dynamics is dominated by the Brillouin peak, which contrasts the spectrum at lower temperatures where the Rayleigh peak is clearly visible. The latter is the behavior observed in liquid-phase Lennard-Jones systems, and, importantly, it means that different underlying processes of the model are governing the dynamics depending on the temperature. Finally, the self-part of the intermediate scattering function is compared to the predictions of the diffusion equation; this also reveals that single particle dynamics are not correctly captured by the continuum theory at high temperatures. In conclusion, we recommend that in order for the o-DPD model to be applicable to study hydrodynamic phenomena, the system must be away from the gas-like region in phase space, that is, the Schmidt number must be well above unity.

* jschmidt@ruc.dk

I. INTRODUCTION

The dissipative particle dynamics (DPD) method [1, 2] is widely used to perform mesoscale computer simulations of, e.g., polymer solutions [3], spinodal decomposition [4], and fluid flows in micro- and nanopores [5, 6], just to name a few examples. A standard DPD simulation involves a set of point mass particles interacting by three different forces; a conservative, a dissipative, and a random force in such a manner that momentum is conserved. The DPD particle can be thought of as a collection of molecules moving in a coherent fashion [7]. The forces are often tweaked to mimic specific fluidic systems, e.g., the particles can be connected with spring forces to simulate polymer solutions and melts; see for example the review by Moeendarbary *et al.* [8]. Importantly, the interparticle conservative force is weak and usually without a strong repulsive core, which gives rise to a large compressibility and zero excluded volume.

In the original DPD model, here denoted o-DPD, the conservative force is linear with respect to the distance between the two point masses [9]. This model is simple and very appealing; however, it yields an unrealistic equation of state which is quadratic in density [9]. Also, the dissipative force depends only on the position and velocity differences of the two interacting particles and neglects shear forces [10]. Even for the o-DPD model, the parameter space is quite large and the physical interpretation of parameters is not always straightforward. For example, the particle density can be chosen as a *free* parameter for a given system, and from this choice the conservative force parameter can be estimated using the compressibility [9]. Interestingly, this so-called adaptive approach leads to a decreasing viscosity for decreasing temperature [5], which characterizes a gas [11]. This gaseous behavior is also manifested by a Schmidt number of order unity [9]. (The Schmidt number is defined as the ratio between the kinematic viscosity and diffusion coefficient.) Despite a lot of effort and many extensions and modifications to the DPD method [10], likely due to its simplicity the o-DPD model is used by the simulation community to simulate hydrodynamic phenomena, see for example Refs. [5, 12–14].

Because of the features mentioned above, Español and Warren refer to the o-DPD model as a toy model, which can nevertheless be used for simulations of fluctuating hydrodynamics [10]. This is perhaps surprising knowing that classical hydrodynamics breaks down for gasses, i.e., in the limit of large mean-free path compared to the characteristic length scale of the

system, i.e., large Knudsen number [15]. To our knowledge, no systematic investigation of the o-DPD model has been carried out in the framework of fluctuating hydrodynamics, which is what we seek to do here.

We base our investigation on Onsager's regression hypothesis, which states that the regression of microscopically induced fluctuations in equilibrium follows the macroscopic laws of small non-equilibrium disturbances [16], i.e., thermally induced perturbations relax according to hydrodynamics. Typically, these relaxations do not refer to hydrodynamic quantities like density and momentum directly, but instead to the decay of the associated correlation functions [17], as predicted by hydrodynamic theory. We derive these correlation functions from fluctuating hydrodynamics as this may not be known to the reader; also, we present it in a slightly different form (albeit equivalent) from that of standard texts [15, 18, 19]. To make the study manageable, we focus on a limited part of the parameter space of the o-DPD model.

II. THE HYDRODYNAMIC RELAXATION FUNCTIONS

The hydrodynamic quantities we study here are the mass density, $\rho = \rho(\mathbf{r}, t)$, the streaming velocity, $\mathbf{u} = \mathbf{u}(\mathbf{r}, t)$, and the excess kinetic energy per unit mass, $e = e(\mathbf{r}, t)$; this latter quantity is defined as the difference between the local kinetic and average kinetic energy per particle, $me(\mathbf{r}, t) = E_{\text{kin}}(\mathbf{r}, t) - \langle E_{\text{kin}} \rangle$, where m is the mass and $\langle \ldots \rangle$ denotes the ensemble average. Based on the microscopic hydrodynamic operator formalism [20] one can derive the following the balance equations

$$\frac{\partial \rho}{\partial t} = -\boldsymbol{\nabla} \cdot \mathbf{J}^m - \boldsymbol{\nabla} \cdot (\rho \mathbf{u}) \tag{1a}$$

$$\frac{\partial \rho \mathbf{u}}{\partial t} = -\boldsymbol{\nabla} \cdot \mathbf{P} - \boldsymbol{\nabla} \cdot (\rho \mathbf{u}\mathbf{u}) \tag{1b}$$

$$\frac{\partial \rho e}{\partial t} = \sigma_e - \boldsymbol{\nabla} \cdot \mathbf{J}^e - \boldsymbol{\nabla} \cdot (\rho e \mathbf{u}) \tag{1c}$$

where $\mathbf{J}^m$ is the mass flux tensor due to density gradients, $\mathbf{P}$ is the pressure tensor, and $\mathbf{J}^e$ the excess kinetic energy flux tensor. The excess kinetic energy is not a conserved quantity; hence, the production term σ_e appearing in Eq. (1c). Furthermore, for the mass balance equation, Eq. (1a), we have decomposed the mass flux into two parts; one due thermal motion (a diffusive process), $\mathbf{J}^m$, and one due to the fluid advective motion, $\rho \mathbf{u}$.

The three quantities can be written as the sum of average and fluctuating parts, i.e., $\rho = \rho_{\rm av} + \delta\rho$, $\mathbf{u} = \delta\mathbf{u} = (\delta u_x, \delta u_y, \delta u_z)$, and $e = \delta e$ since the averages of the streaming velocity and excess kinetic energy are zero. To first order in the fluctuations we have that

$$\rho\mathbf{u} = (\rho_{\rm av} + \delta\rho)\delta\mathbf{u} \approx \rho_{\rm av}\delta\mathbf{u} \quad \text{and} \quad \rho e \approx \rho_{\rm av}\delta e\,. \tag{2}$$

Using the framework of fluctuating hydrodynamics, [21] we now introduce the linear constitutive relations with stochastic forcing

$$\mathbf{J}^m = -D\boldsymbol{\nabla}\rho + \delta\mathbf{J}^m \tag{3a}$$

$$\mathbf{P} = (p_{eq} - \eta_v(\boldsymbol{\nabla}\cdot\mathbf{u}))\,\mathbf{I} - 2\eta_0\,(\overset{os}{\boldsymbol{\nabla}}\mathbf{u}) + \delta\mathbf{P} \tag{3b}$$

$$\mathbf{J}^e = -\frac{\lambda}{c_V}\boldsymbol{\nabla}e + \delta\mathbf{J}^e \tag{3c}$$

where D is the mass flux diffusivity coefficient, p is the normal pressure, η_v and η_0 the bulk and shear viscosities, λ the heat conductivity, c_V the specific heat at constant volume, and $(\overset{os}{\boldsymbol{\nabla}}\mathbf{u})$ is the trace-less symmetric part of the strain rate tensor.

Equations (3b) and (3c) are just Newton's law of viscosity and Fourier's law of conduction with added stochastic forcing. However, as we cannot in general ignore cross-correlation effects on small time and length scale, it is noted that D is not the self-diffusion coefficient [22]. As the mass density and excess kinetic energy are scalars, that is of the same parity, both fluxes in Eqs. (3a) and (3c) can be dependent on the gradients of ρ and e according to Courier's principle [23]. Here we follow Alley and Alder [18] and model the cross coupling through the production term σ_e and the pressure p_{eq}.

In equilibrium the stochastic forcing term has a zero average [21] and is uncorrelated with the hydrodynamic quantities, e.g., $\langle\delta\mathbf{J}^m(\mathbf{r},t)\delta\mathbf{u}(\mathbf{r}',t')\rangle = \mathbf{0}$. Substituting Eqs. (2) and (3) into Eq. (1), we arrive at the stochastic dynamics to first order in the fluctuations

$$\frac{\partial\delta\rho}{\partial t} = D\nabla^2\delta\rho - \rho_{\rm av}\boldsymbol{\nabla}\cdot\delta\mathbf{u} - \boldsymbol{\nabla}\cdot\delta\mathbf{J}^m \tag{4a}$$

$$\rho_{\rm av}\frac{\partial\delta\mathbf{u}}{\partial t} = -\boldsymbol{\nabla}\delta p_{eq} + (\eta_v + \eta_0/3)\boldsymbol{\nabla}(\boldsymbol{\nabla}\cdot\delta\mathbf{u}) + \eta_0\nabla^2\delta\mathbf{u} - \nabla\cdot\delta\mathbf{P} \tag{4b}$$

$$\rho_{\rm av}\frac{\partial\delta e}{\partial t} = \sigma_e + \frac{\lambda}{c_V}\nabla^2\delta e - \boldsymbol{\nabla}\cdot\delta\mathbf{J}^e \tag{4c}$$

since the advective terms are of second order. For local thermodynamic equilibrium, the pressure fluctuations can be written as [19]

$$\delta p = \left(\frac{\partial p}{\partial\rho}\right)_T\delta\rho + \left(\frac{\partial p}{\partial T}\right)_\rho\delta T = \frac{1}{\rho_{\rm av}\chi_T}\delta\rho + \frac{\beta_V}{c_V}\delta e\,, \tag{5}$$

where $\chi_T = -1/V\,(\partial V/\partial p)_T$ is the isothermal compressibility and $\beta_{\rm V} = (\partial p/\partial T)_\rho$ is the thermal pressure coefficient. The production term for the excess kinetic energy is given by Alley and Alder [18]

$$\sigma_e = \frac{T\beta_{\rm V}}{\rho_{\rm av}}\frac{\partial \delta\rho}{\partial t} = \frac{T\beta_{\rm V}}{\rho_{\rm av}}\left(D\nabla^2\delta\rho - \rho_{\rm av}\boldsymbol{\nabla}\cdot\delta\mathbf{u} - \boldsymbol{\nabla}\cdot\delta\mathbf{J}^m\right). \tag{6}$$

Defining the Fourier transform as

$$\widetilde{f}(\mathbf{k},t) = \iiint_{-\infty}^{\infty} f(\mathbf{r},t)\,e^{-i\mathbf{k}\cdot\mathbf{r}}\,\mathrm{d}\mathbf{r} \tag{7}$$

and then substituting Eqs. (5) and (6) into Eq. (4) gives, in Fourier space,

$$\frac{\partial\widetilde{\delta\rho}}{\partial t} = -Dk^2\widetilde{\delta\rho} - i\rho_{\rm av}\mathbf{k}\cdot\widetilde{\delta\mathbf{u}} - i\mathbf{k}\cdot\widetilde{\delta\mathbf{J}}^m \tag{8a}$$

$$\rho_{\rm av}\frac{\partial\widetilde{\delta\mathbf{u}}}{\partial t} = -\frac{i\mathbf{k}}{\rho_{\rm av}\chi_T}\widetilde{\delta\rho} - (\eta_v+\eta_0/3)\mathbf{k}(\mathbf{k}\cdot\widetilde{\delta\mathbf{u}}) - \eta_0k^2\widetilde{\delta\mathbf{u}} - \frac{i\beta_v\mathbf{k}}{c_V}\widetilde{\delta e} - i\mathbf{k}\cdot\widetilde{\delta\mathbf{P}} \tag{8b}$$

$$\rho_{\rm av}\frac{\partial\widetilde{\delta e}}{\partial t} = -\frac{T\beta_V Dk^2}{\rho_{\rm av}}\widetilde{\delta\rho} - iT\beta_V\mathbf{k}\cdot\delta\boldsymbol{u} - \frac{\lambda k^2}{c_V}\widetilde{\delta e} - i\mathbf{k}\cdot\left(\widetilde{\delta\mathbf{J}}^e + \widetilde{\delta\mathbf{J}}^m\right) \tag{8c}$$

This holds for any sufficiently small wavevector $\mathbf{k}$. If one makes a particular simple choice for the wavevector, then the dynamics can be decomposed into transverse (normal) and longitudinal (parallel) dynamics with respect to this wavevector. For example, if we select $\mathbf{k} = (0,k,0)$, then from Eq. (8) the transverse dynamics is given by the streaming velocity components $\widetilde{\delta u_x}$ and $\widetilde{\delta u_z}$ via

$$\frac{\partial\widetilde{\delta u_x}}{\partial t} = -\nu_0k^2\widetilde{\delta u_x} - \frac{ik}{\rho_{\rm av}}\widetilde{\delta P_{yx}} \tag{9a}$$

$$\frac{\partial\widetilde{\delta u_z}}{\partial t} = -\nu_0k^2\widetilde{\delta u_z} - \frac{ik}{\rho_{\rm av}}\widetilde{\delta P_{yz}} \tag{9b}$$

where $\nu_0 = \eta_0/\rho_{\rm av}$ is the kinematic viscosity. It is seen that Eqs. (9a) and (9b) are identical with respect to the dynamics and that the transverse dynamics are independent of the energy and density fluctuations. The longitudinal dynamics is given by

$$\frac{\partial\widetilde{\delta\rho}}{\partial t} = -Dk^2\widetilde{\delta\rho} - i\rho_{\rm av}k\widetilde{\delta u_y} - ik\widetilde{\delta J_y^m} \tag{10a}$$

$$\frac{\partial\widetilde{\delta u_y}}{\partial t} = -\frac{ik}{\rho_{\rm av}^2\chi_T}\widetilde{\delta\rho} - \nu_lk^2\widetilde{\delta u_y} - \frac{ik\beta_V}{c_V\rho_{\rm av}}\widetilde{\delta e} - \frac{ik}{\rho_{\rm av}}\widetilde{\delta P_{yy}} \tag{10b}$$

$$\frac{\partial\widetilde{\delta e}}{\partial t} = -\frac{T\beta_V Dk^2}{\rho_{\rm av}^2}\widetilde{\delta\rho} - \frac{iT\beta_V k}{\rho_{\rm av}}\widetilde{\delta u_y} - \kappa k^2\widetilde{\delta e} - \frac{ik}{\rho_{\rm av}}\left(\widetilde{\delta J_y^e} + \widetilde{\delta J_y^m}\right) \tag{10c}$$

where $\nu_l = (\eta_v + \eta_0/3)/\rho_{\rm av}$ is the longitudinal kinematic viscosity and $\kappa = \lambda/(c_V \rho_{\rm av})$.

As mentioned above, one usually does not study the fluctuating quantities directly, but rather the associated correlation functions. To this end we define the equilibrium time-correlation function between quantities A and B as

$$C_{AB}(\mathbf{k}, t) = \frac{1}{V} \langle A(\mathbf{k}, t) B(-\mathbf{k}, 0) \rangle \ , \tag{11}$$

where V is the system volume. Thus, multiplying Eqs. (9a) with $\widetilde{\delta u}_x(-k, 0)$ and taking the ensemble average over initial conditions leads to

$$\frac{\partial C_{uu}^{\perp}}{\partial t} = -\nu_0 k^2 C_{uu}^{\perp} \tag{12}$$

for the transverse relaxation. Here $C_{uu}^{\perp} = \langle \widetilde{\delta u}_x(k, t) \widetilde{\delta u}_x(-k, 0) \rangle / V$ is the transverse velocity autocorrelation function, and we have used that the stochastic forcing term is uncorrelated with the fluctuating quantities. The solution to Eq. (12) is

$$C_{uu}^{\perp}(k, t) = \frac{k_B T}{\rho_{\rm av}} e^{-\nu_0 k^2 t} \, , \tag{13}$$

where the initial value $C_{uu}^{\perp}(k, 0) = k_B T / \rho_{\rm av}$ is found by assuming equipartition.

From Eq. (10) one can form nine coupled correlation functions for the longitudinal dynamics. For example, dynamic equations for $C_{\rho\rho}, C_{\rho u}, C_{\rho e}$ are formed by multiplying Eq. (10a) with $\delta\widetilde{\rho}(-\mathbf{k}, 0), \delta\widetilde{u}(-\mathbf{k}, 0)$, and $\delta\widetilde{e}(-\mathbf{k}, 0)$, respectively, and taking the ensemble average. In matrix notation, this yields a coupled linear differential equation system for all nine correlation functions

$$\frac{\mathrm{d}}{\mathrm{dt}} \begin{bmatrix} C_{\rho\rho} & C_{\rho u} & C_{\rho e} \\ C_{u\rho} & C_{uu} & C_{ue} \\ C_{e\rho} & C_{eu} & C_{ee} \end{bmatrix} = - \begin{bmatrix} Dk^2 & i\rho_{\rm av} k & 0 \\ \frac{ik}{\rho_{\rm av}^2 \chi_T} & \nu_l k^2 & \frac{ik\beta_V}{c_V \rho_{\rm av}} \\ \frac{T\beta_V D k^2}{\rho_{\rm av}^2} & \frac{iT\beta_V k}{\rho_{\rm av}} & \kappa k^2 \end{bmatrix} \begin{bmatrix} C_{\rho\rho} & C_{\rho u} & C_{\rho e} \\ C_{u\rho} & C_{uu} & C_{ue} \\ C_{e\rho} & C_{eu} & C_{ee} \end{bmatrix} . \tag{14}$$

The coefficient matrix is referred to as the hydrodynamic matrix [19]. By performing the matrix multiplication in Eq. (14) it can be seen that the longitudinal dynamics can be divided into three sets of co-dependent correlation functions, for example, $\dot{C}_{\rho\rho} = A_1(C_{\rho\rho}, C_{u\rho})$, $\dot{C}_{u\rho} = A_2(C_{\rho\rho}, C_{u\rho}, C_{e\rho})$, and $\dot{C}_{e\rho} = A_3(C_{\rho\rho}, C_{u\rho}, C_{e\rho})$, where A_1, A_2 and A_3 are linear functions represented by the hydrodynamic matrix. The three sets are written as triplets

$$\{C_{\rho\rho}, C_{u\rho}, C_{e\rho}\}, \ \{C_{uu}, C_{\rho u}, C_{eu}\}, \text{ and } \{C_{ee}, C_{\rho e}, C_{ue}\} \tag{15}$$

and each set of coupled differential equations can be solved from the hydrodynamic matrix. Up to second order in wavevector, the solution for any of the nine correlation functions has the form

$$C_{AB}(\mathbf{k},t) = K_1 e^{\lambda_1 k^2 t} + e^{\lambda_2 k^2 t}\left[K_2\cos(c_s k t) + iK_3\sin(c_s k t)\right] \tag{16}$$

where

$$\lambda_1 = -\frac{\kappa}{\chi_T \rho_{\rm av} c_s^2}\ ,\ \lambda_2 = \frac{1}{2}\left[\frac{\kappa}{\chi_T \rho_{\rm av} c_s^2} - (D + \nu_l + \kappa)\right]\ , \tag{17}$$

and c_s defined via

$$c_s^2 = \frac{\beta_V^2 \chi_T T - \rho_{\rm av} c_V}{\chi_T c_V \rho_{\rm av}^2} \tag{18}$$

is the adiabatic speed of sound. The three integrating factors K_1, K_2, and K_3 are found from the initial conditions and are, in fact, not independent. Now, C_{AB} is either a real or purely imaginary valued function, which means that if $K_3 = 0$ then in general $K_2 \neq 0$ and $K_1 \neq 0$ while if $K_3 \neq 0$ then $K_2 = K_1 = 0$. In the case where C_{AB} is real, the normalized correlation function is written in the form

$$C_{AB}^N(\mathbf{k},t) = K_{AB} e^{\lambda_1 k^2 t} + (1 - K_{AB}) e^{\lambda_2 k^2 t}\cos(c_s k t)\,. \tag{19}$$

Thus, the longitudinal dynamics is governed by three fundamental processes with frequencies $\lambda_1 k^2, \lambda_2 k^2$, and $c_s k$. From Eq. (17), one sees that the λ_1-process pertains to the thermal diffusion and that the λ_2-process dampens the wave propagation with speed c_s; the magnitude of this damping is governed by all three diffusive processes, i.e., by D, ν_l, and κ. Equations (13) and (19) form the framework for this hydrodynamics study.

III. SIMULATION METHODOLOGY

The o-DPD model is composed of a single type of point mass particle. The particle position, $\mathbf{r}_i$, and momentum, $\mathbf{p}_i$, follow Newton's equation of motion,

$$\frac{\mathrm{d}\mathbf{r}_\mathrm{i}}{\mathrm{dt}} = \frac{\mathbf{p}_i}{m} \tag{20a}$$

$$\frac{\mathrm{d}\mathbf{p}_\mathrm{i}}{\mathrm{dt}} = \mathbf{F}_i \tag{20b}$$

m is the particle mass and $\mathbf{F}_i$ is the total force acting on the DPD particle. The total force is composed of the conservative force, $\mathbf{F}_i^C$, due to the interaction between the particles, a

random force, $\mathbf{F}_i^R$, simulating the coarse graining of many degrees of freedom, and a dissipative force, $\mathbf{F}_i^D$, removing the viscous heating generated from the random force. Thus $\mathbf{F}_i = \mathbf{F}_i^C + \mathbf{F}_i^R + \mathbf{F}_i^D$. As it is common practise, we use reduced units such that the characteristic mass and length scales are set to unity. In reduced units the conservative force is

$$\mathbf{F}_{ij}^C = a_{ij}(1 - r_{ij})\hat{\mathbf{r}}_{ij}\,, \tag{21}$$

where a_{ij} is a parameter that quantifies the repulsion between particles i and j, $\mathbf{r}_{ij}$ is the vector of separation $\mathbf{r}_i - \mathbf{r}_j$, $r_{ij} = |\mathbf{r}_{ij}|$, $\hat{\mathbf{r}}_{ij} = \mathbf{r}_{ij}/r_{ij}$. Here we use $a_{ij} = 25$ and the interactions are ignored when $r_{ij} > 1$. Following Groot and Warren [9], the random force is $\mathbf{F}_{ij}^R = \xi\zeta\sqrt{w(r_{ij})/\Delta t}\,\hat{\mathbf{r}}_{ij}$, where ξ is the random force amplitude, ζ is a uniformly distributed random number with zero mean and unit variance, $w(r_{ij})$ is a weighing function given by $w(r_{ij}) = (1 - r_{ij})^2$. Finally, $\Delta t = 0.01$ is the time step used in the integrator. The dissipative force is $\mathbf{F}_{ij}^D = -\frac{1}{2k_BT^2}w(r_{ij})(\hat{\mathbf{r}}_{ij} \cdot (\mathbf{v}_i - \mathbf{v}_j))\hat{\mathbf{r}}_{ij}$, where $\mathbf{v}$ is the particle velocity. In all simulations, the amplitude ξ is set to 3.0. The equations of motion are integrated forward in time using the standard velocity Verlet algorithm by Groot and Warren [9]. We note that this algorithm yields a kinetic temperature above the target temperature. The system size is 1000 particles at density $\rho_{\text{av}} = 3.0$, and temperatures in the range $0.13 \leq T \leq 1.07$ are simulated (corresponding to thermostat target temperatures of 0.1 to 1).

During the simulations, all 10 correlation functions are evaluated from the microscopic definition of the hydrodynamic variables, which to first order in fluctuations are

$$\widetilde{\rho}(\mathbf{k}, t) = \sum_i m e^{-\mathbf{k}\cdot\mathbf{r}_i(t)} \tag{22a}$$

$$\widetilde{\delta\mathbf{u}}(\mathbf{k}, t) = \frac{1}{\rho_{\text{av}}} \sum_i \mathbf{v}_i e^{-\mathbf{k}\cdot\mathbf{r}_i(t)} \tag{22b}$$

$$\widetilde{\delta e}(\mathbf{k}, t) = \frac{1}{\rho_{\text{av}}} \left[\sum_i \frac{1}{2} m v_i^2 e^{-\mathbf{k}\cdot\mathbf{r}_i(t)} - \langle E_{\text{kin}} \rangle \right] \tag{22c}$$

The pressure tensor at zero wavevector is also evaluated using the Irving-Kirkwood definition [24] as

$$\mathbf{P}(t) = \frac{1}{V} \left[\sum_i \frac{\mathbf{p}_i \mathbf{p}_i}{m_i} + \sum_i \sum_{j>i} \mathbf{r}_{ij} \mathbf{F}_{ij}^C \right] . \tag{23}$$

Note that the pressure excludes the dissipative and random force contributions [9]; we address this later. The frequency-dependent viscosity (or complex viscosity) is calculated from

the shear components by the Fourier-Laplace transform of the Green-Kubo integral,

$$\eta^*(\omega) = \frac{V}{3k_BT}\int_0^\infty \sum_{\alpha\beta}\langle P_{\alpha\beta}(t)P_{\alpha\beta}(0)\rangle\, e^{-i\omega t}\,\mathrm{dt}\,, \tag{24}$$

where the double index $\alpha\beta$ runs over the xy, xz, and yz components of the pressure tensor. The self-diffusivity coefficient is evaluated from the Green-Kubo integral of the single particle velocity autocorrelation function. We will use both the dynamic viscosity, η^*, and kinematic viscosity, $\nu^* = \eta^*/\rho_{\mathrm{av}}$, whenever one is more convenient than the other.

In a few cases, the dynamics of the o-DPD model are compared to a liquid-phase Lennard-Jones system at the state-point $(\rho, T) = (0.85, 1.121)$ in units of σ^3 and k_B/ϵ. The Lennard-Jones particles interact through the standard shifted 12-6 potential [25] using a cut-off distance at $r/\sigma = 2.5$. The system size is $N = 1000$, and the equations of motion are integrated forward in time using a leap-frog method [26]. To control the temperature, the Nose-Hoover thermostat [27, 28] is applied. The dynamic properties are calculated as explained above.

IV. RESULTS

It is informative to show the fluid structure of the different state points investigated. Figure 1 (a) plots the radial distribution functions for three state points, namely, $T = 1.07$, 0.36, and 0.13. The structure can be compared to the corresponding transport properties in Table I and Fig. 1 (b : First, one sees that the Schmidt number Sc= $\nu_0/D_s \approx 1$ for $T > 0.5$ and the viscosity in the zero-frequency limit decreases with decreasing temperature, which is the well-known gas-like behavior [11]. In agreement with this, the radial distribution function shows very little fluid structure. At low temperature $T = 0.13$, there is a fluid structure and Sc = 53. For reference, the Lennard-Jones liquid state point is characterized by Sc $\approx$ 50. It is interesting that for $T = 0.36$ a fluid structure is also present, yet the viscosity is almost unchanged compared to $T = 1.07$. The state points then span a gas-like state and a liquid-like state for the repulsion and friction parameters chosen here. Again we note that high temperatures are frequently used to simulate hydrodynamic phenomena, such as a recent study in Ref. 5.

To compare the mechanical data directly with a simple predictive model, we study the complex shear modulus $G^* = i\omega\eta^*$, which is plotted in Fig. 2 (a) for $T = 1.07$ and 0.13.

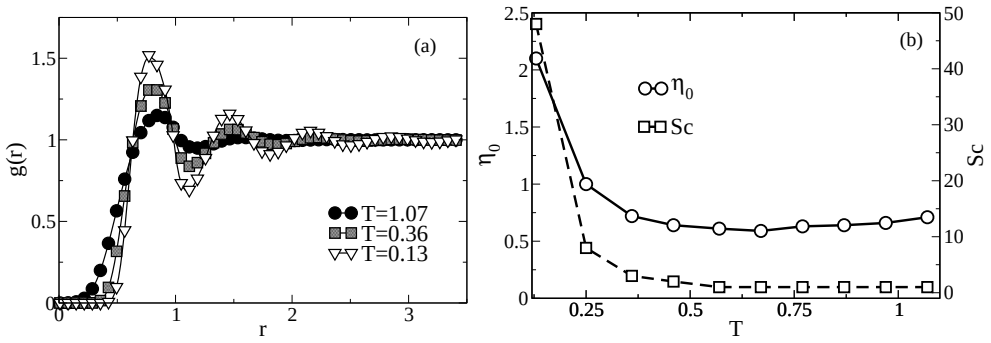

FIG. 1. (a) Radial distribution function for the o-DPD system at $T = 1.07$, 0.36, and 0.13. (b) The zero frequency shear viscosity $\eta_0 = \lim_{\omega\to 0}\eta^*(\omega)$ and the Schmidt number Sc as functions of temperature. The Schmidt number is defined as $\mathrm{Sc} = \eta_0/(\rho_{\mathrm{av}} D_s) = \nu_0/D_s$, where D_s is the self-diffusion coefficient and ν_0 the kinematic viscosity. Statistical uncertainties are of the magnitude of the symbol sizes. Lines serve as guides to the eye.

T	1.07	0.97	0.87	0.77	0.67	0.57	0.46	0.36	0.25	0.13
η_0	0.71	0.66	0.64	0.63	0.66	0.61	0.64	0.75	1.00	2.10
τ_M	0.056	0.056	0.056	0.059	0.064	0.073	0.088	0.115	0.167	0.313
D_s	0.32	0.28	0.25	0.22	0.18	0.15	0.11	0.078	0.045	0.015
G_∞	12.7	12.0	11.5	10.6	9.3	8.3	7.3	6.3	6.0	6.7
Sc	1	1	1	1	1	1	2	3	8	48

TABLE I. Table of the viscosity η_0, the Maxwell relaxation time τ_M, the self-diffusivity D_s, instantaneous shear modulus G_∞, and the Schmidt number Sc for the temperatures studied. Density $\rho = 3.0$ in all simulations.

Data are compared to a single-element Maxwell model

$$G^*(\omega) = \frac{i\omega G_0}{i\omega + \tau_M^{-1}} \tag{25}$$

using amplitude G_0 and the Maxwell characteristic time τ_M as fitting parameters. The instantaneous shear modulus (infinite-frequency complex shear modulus), G_∞, can then be found from the relation $\eta_0/\tau_M = G_\infty$. From Fig. 2 (a) it is seen that for $T = 0.13$ and

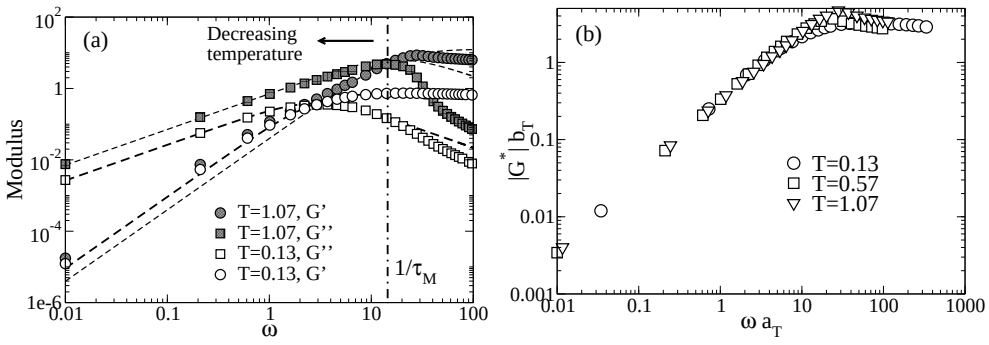

FIG. 2. (a) The complex shear modulus $G^* = G' + iG''$ as a function of frequency for $T = 1.07$ and $T = 0.13$. Symbols are transformed simulation results and dashed lines are fits to the Maxwell model, Eq. (25), for $T = 0.13$ (thick line) and $T = 1.07$ (thin line). The arrow indicates that the inverse Maxwell time (G" peak frequency) decreases for decreasing temperature. (b) Test of time-temperature superposition using the magnitude of the shear modulus. Shift factors are defined as $a_T = \eta_0(T)/\eta_0(T_{\rm ref})$ and $b_T = T_{\rm ref}/T$, where $T_{\rm ref} = 0.13$.

$\omega < 20$ the o-DPD model is Maxwellian, or equivalently, that the shear relaxation follows a simple exponential decay for $t > \pi/10$. This is not the case at higher temperatures; here the higher magnitude at lower frequencies (compared to the Maxwell model) and the decrease in magnitude at the highest frequencies indicate that the real part of the modulus is clearly non-Maxwellian. From Table I it is seen that the relaxation time τ_M increases monotonically for decreasing temperature. This in turn implies that G_∞ decreases with decreasing temperature; this is a surprising result as one would expect the repulsive forces that counteract an external shear stress to be less affected by thermal perturbations at low temperatures [15]. We also test for time-temperature superposition (TTS) in Fig. 2(b). Here the frequency is scaled by a factor $a_T = \eta_0(T)/\eta_0(T_{\rm ref})$ and the magnitude of G^* by $b_T = T_{\rm ref}/T$ [29], where the reference temperature is $T_{\rm ref} = 0.13$. TTS applies for low frequencies, below $\omega \approx 1/\tau_M$.

Next we turn to the non-zero wavevector regime. Bocquet and Charlaix [30] argued that hydrodynamics is valid for wavevectors

$$k < \sqrt{\frac{2\pi}{\nu_0 \tau_s}}\,, \tag{26}$$

where τ_s is the time when the shear pressure autocorrelation function is decayed [20]. This relation has been shown to work quite well for a molecular dumbbell model [20]. For $T =$

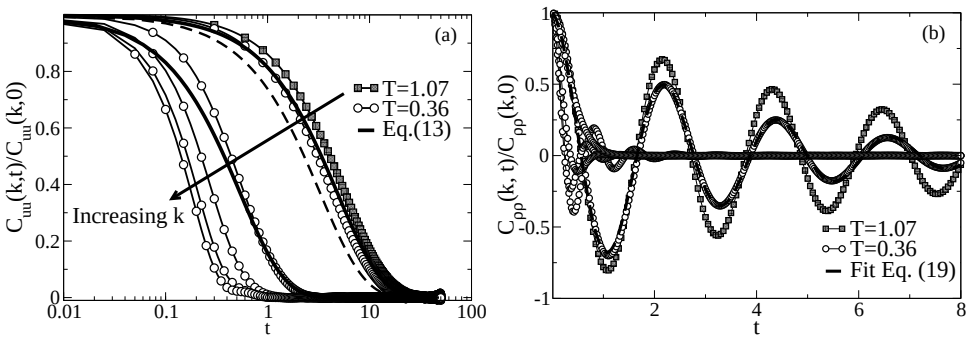

FIG. 3. (a) The transverse velocity autocorrelation function $C^{\perp}_{uu}$ in the wavevector interval interval $0.91 \leq k \leq 8.19$ for $T = 0.36$ and $k = 0.91$ for $T = 1.07$. Symbols connected with lines are simulation results, and thick lines show predictions from Eq. (13) for wavevectors $k = 0.91$ and 2.73 using $\eta_0 = 0.75$. The dashed line is the theoretical prediction for $\eta_0 = 1.1$. (b) The density autocorrelation function in the wavevector interval $0.91 \leq k \leq 8.19$ for $T = 0.36$. For $T = 1.07$ only data for $k = 0.91$ are shown. Circles connected with lines are simulation results, and a thick dashed line shows the best fit of data to Eq. (19), which gives $K_{\rho\rho} = 0.04, \lambda_1 = -1.1, \lambda_2 = -0.41$, and $c_s = 3.1$.

0.36, $\tau_s \approx 1.5$ indicates an upper limit of around $k \approx 4$, and for $T = 1.07$ $\tau_s \approx 2.2$ giving $k \approx 2$.

With this in mind, we plot in Fig. 3 (a) the normalized transverse velocity autocorrelation for different wavevectors. Data for temperatures $T = 1.07$ and $T = 0.36$ are shown; these two state points have approximately same viscosity and therefore $C^{\perp}_{uu}$ should, according to Eq. (13) and Table I, relax with the same characteristic time scale. The relaxation is slower than predicted by the theory for the high temperature state point, whereas the predictions are good in the low temperature regime. This is surprising as the Schmidt number is approximately the same, indicating both are gaseous state points. Using the Bocquet-Charlaix criterion in Eq. (26), $k = 0.91$ is within both validity limits, and hence one expects hydrodynamics to be valid. For $T = 0.36$, the prediction fails already at $k = 2.73$ for small times and the Bocquet-Charlaix criterion is not readily applicable. It is also worth noting that for a given wavevector the relaxation is identical within statistical uncertainty for all studied wavevectors when $T > 0.5$; this is in qualitative agreement with the theory.

The transverse velocity autocorrelation provides an opportunity to compare contributions to the pressure tensor. If the total force is used in the definition of the pressure tensor, Eq.

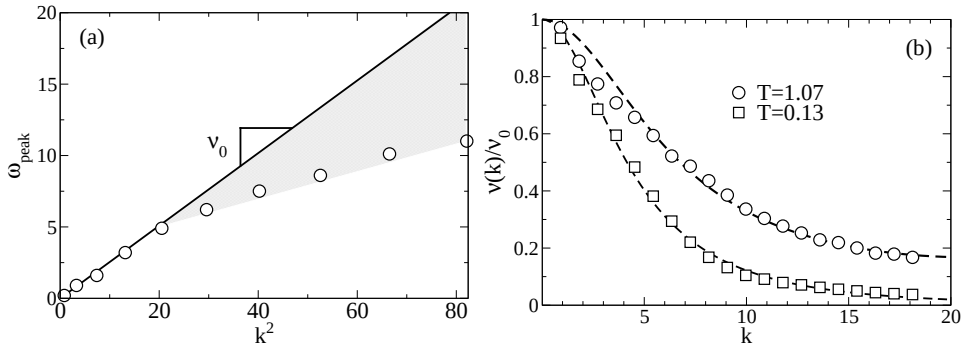

FIG. 4. (a) Scaling of ω_{Peak} with k^2 for $T = 1.07$. The line is the best fit to data for $k < 6.0$; the viscosity is given by the slope. Shaded area indicates the deviation between predictions and data. (b) Viscosity kernel at temperatures $T = 0.13$ and $T = 1.07$. The dashed lines are best fits using Eq. (29).

(23), then the shear pressure autocorrelation function features a spike at $t = 0$ because the random force $\mathbf{F}^R$ contributes an instantaneous correlation. The Green-Kubo integral therefore yields a higher shear viscosity. For $T = 0.36$ and a time step of 0.01, $\eta_0 = 1.1$ if all force contributions are included in the pressure tensor. The resulting relaxation of the transverse velocity autocorrelation predicted by the theory is shown as the dashed line in Fig. 3 (a). Clearly, including all forces overestimates the relaxation. This motivates our choice to include only the conservative part of the force in the pressure tensor definition. Furthermore, as one decreases the integrator time step the spike appears to converge to the Dirac delta as expected, however, due to numerical limitations the resulting viscosity then depends on the sample time step chosen.

Normalizing Eq. (13) with respect to $C^{\perp}_{uu}(\mathbf{k}, 0)$ and applying a Fourier-Laplace transform leads in the frequency domain to

$$\widehat{C}^{\perp,N}_{uu}(\mathbf{k},\omega) = \int_0^\infty e^{-\nu_0 k^2 t} e^{-i\omega t} \mathrm{dt} = \frac{1}{\nu_0 \mathrm{k}^2 + \mathrm{i}\omega}\,, \tag{27}$$

which gives a peak in the imaginary part of the spectrum at $\omega_{\mathrm{peak}} = \nu_0 k^2$. This peak frequency is plotted in Fig. 4 (a) for $T = 1.07$. For small wavevectors, the peak frequency follows the predictions from the classical hydrodynamic theory: ω_{peak} is proportional to k^2 and the relaxation is governed by the diffusion of momentum. The prediction fails for $k > 6$. The frequency and wavevector dependent shear viscosity can be defined by re-arranging Eq.

(27),

$$\widehat{\nu}(k,\omega) = \frac{1 - i\omega \widehat{C}^{\perp,N}_{uu}(\mathbf{k},\omega)}{k^2 \widehat{C}^{\perp,N}_{uu}(\mathbf{k},\omega)} \,. \tag{28}$$

This result can also be derived from first principles by including the position and time dependence of the transport coefficient in Eqs. (3). In the zero frequency limit we have the viscosity kernel $\widetilde{\nu}(k) = 1/k^2 \widehat{C}^{\perp,N}_{uu}(\mathbf{k},0)$. Figure 4 (b) shows this viscosity kernel at zero frequency for $T = 1.07$ and $T = 0.13$. Following previous work [31], the dashed line is the best fit of the equation Lorentzian type empirical model

$$\widetilde{\nu}(k) = \frac{\nu_0}{1 + \alpha k^\beta} \,, \tag{29}$$

to data using α and β as fitting parameters; ν_0 is found from Table I and is not a fitting parameter. It is worth noting that this empirical form for the kernel fits molecular dynamics data for a range of different liquids [20, 31]. It is, however, not able to capture the kernel for high temperatures and $k < 5$ in the o-DPD system.

It is interesting to see that for k less than unity, the wavevector-dependent viscosity reaches ν_0, i.e., for $k < 1.0$ the local Newtonian law of viscosity holds. Using the o-DPD parametization for water of Boromand et al. [5] where the unit of length is 6.45 Å ($k < 0.15\text{Å}^{-1}$), this corresponds to a length scale, $l = 2\pi/k$, of 4-5 nm. This can be compared to detailed atomistic molecular dynamics simulations of water in which $l \approx 2$ nm [20]. To make the two lengths agree, the extent of a single o-DPD particle corresponds to a single water molecule and the mesoscopic assumption for the method is questionable.

Rather than approaching the deviation between theory and simulation through wavevector dependent transport coefficients, one can generalize the stochastic forcing and assume $\delta\mathbf{J}^m$, $\delta\mathbf{P}$, and $\delta\mathbf{J}^e$ to be correlated with hydrodynamic quantities. In this case the transverse dynamics are governed by the equation

$$\frac{\partial C^{\perp}_{uu}}{\partial t} = -\nu_0 k^2 C^{\perp}_{uu} + \varepsilon(\mathbf{k},t) \tag{30}$$

where

$$\varepsilon(\mathbf{k},t) = -\frac{ik}{\rho_{\text{av}} V} \langle \widetilde{\delta P}_{yx}(\mathbf{k},t) \widetilde{\delta u}_x(-\mathbf{k},0) \rangle \neq 0. \tag{31}$$

Applying a Fourier-Laplace transform gives the correlation between forcing and the transverse velocity in terms of wavevector and frequency as

$$\widehat{\varepsilon}(\mathbf{k},\omega) = (i\omega + \nu_0 k^2) \widehat{C}^{\perp}_{uu}(\mathbf{k},\omega) - C^{\perp}_{uu}(\mathbf{k},0) \,. \tag{32}$$

This means that for high temperatures the contribution from ε is significant for all wavevectors, whereas only small length scale correlations are observed at low temperatures.

We now turn to the longitudinal relaxation dynamics. The density autocorrelation function, $C_{\rho\rho}$, is plotted in Fig. 3 (b) for $T = 1.07$ and $T = .036$. It is worth noting that the density autocorrelation function is related to the coherent intermediate scattering function, $F(\mathbf{k}, t)$, by $C_{\rho\rho}(\mathbf{k}, t) = \rho_{\text{av}} F(\mathbf{k}, t)$. The density autocorrelation function is a real-valued function; hence, it relaxes according to Eq. (19). The dashed line is the best fit of Eq. (19) to data for $k = 0.91$ at $T = 0.36$ using $K_{\rho\rho}$, λ_1, λ_2, and c_s as fitting parameters. The damped oscillations predicted from hydrodynamics are evident and the damping is most pronounced at low temperatures, which is likely linked to the increase in viscous dissipation. Also, it is seen that the oscillatory frequencies are roughly the same for the two different temperatures, which means that the speed of sound is to a good approximation independent of temperature. This in turn indicates that χ_T, β_V and c_V are independent of temperature as the speed of sound is given through these thermodynamic coefficients.

For $T > 0.13$, the thermal diffusion process contributes little to the relaxation dynamics, which we attribute to the large compressibility that characterizes soft conservative interactions. This becomes more evident in frequency space where the Fourier-Laplace transform of Eq. (19) leads to

$$\widehat{C}^N_{\rho\rho}(\mathbf{k}, \omega) = \frac{K_{\rho\rho}}{\lambda_1 k^2 + i\omega} - \frac{(1 - K_{\rho\rho})(i\omega - \lambda_2 k^2)}{(c_s k)^2 + (i\omega - \lambda_2 k^2)^2} \tag{33}$$

for the density autocorrelation function. Again, note the two different contributions to the relaxation. The real part of $\widehat{C}^N_{\rho\rho}$ is symmetric about $\omega = 0$ and we therefore only discuss the behaviour for $\omega \geq 0$. The first term gives rise to the Rayleigh peak at $\omega = 0$ and is present at low frequencies. The half-width of the Rayleigh peak is $\lambda_1 k^2$, i.e., it is given by the thermal process. The second term as a maximum at frequency $c_s k$; the maximum is identified as the Brillouin peak and has half width $2\lambda_2 k^2$, i.e., it depends on all three diffusive processes. In Fig. 5, the real part of $\widehat{C}^N_{\rho\rho}$ is plotted for $k = 0.91$ for three different temperatures. The dashed lines are the two different contributions to the relaxation in Eq. (33), and $K_{\rho\rho}$, λ_1, λ_2, and c_s are found from fitting Eq. (19) to data. The relaxation is divided into two different regimes: In the low frequency limit (long time limit), the relaxation is governed by both processes, i.e., both the λ_1 and λ_2-modes, whereas for medium and short times the relaxation is mainly determined by the λ_2-mode. This is different from liquid Lennard-Jones systems,

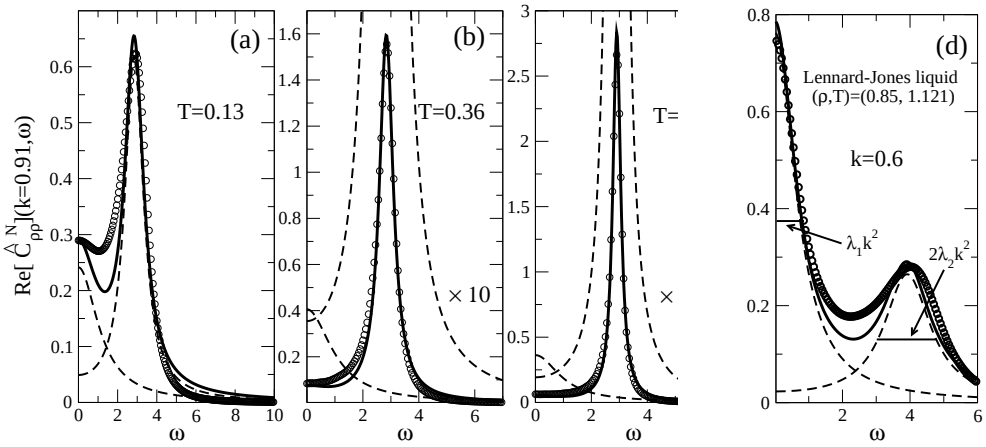

FIG. 5. The real part of $\widehat{C}^N_{\rho\rho}$ at $k = 0.91$ for temperatures (a) 0.13, (b) 0.36, and (c) 1.07. The circles represent simulation data and the punctured lines are the different λ_1- and λ_2-mode contributions to the relaxation; for temperatures $T = 0.36$ and $T = 1.07$ the contributions are multiplied by a factor of 10 for clarity. Full line is the sum of the λ_1 and λ_2 mode contributions. (d) The real part of $\widehat{C}^N_{\rho\rho}$ for the Lennard-Jones system at $k = 0.60$. Here the Rayleigh and Brillouin half peak widths are illustrated.

where the Rayleigh peak is very distinct for low frequencies and the dynamics are completely dominated by the thermal process, see Fig. 5 (d). Again, we attribute the behavior seen in the o-DPD system to the large compressibility. It is not surprising to observe that the Brillouin peak width for $T = 0.13$ is larger than for $T = 1.07$ as the viscosity increases dramatically for low temperatures, Fig. 1 (b), therefore increasing the magnitude of λ_2. The temperature independence of the Brillouin peak position reinforces the point that the temperature independence of the speed of sound c_s. The Rayleigh peak half width on the other hand is roughly independent of temperature, hence, the fraction κ/χ_T is constant with respect to temperature.

Figure 6 shows the density-density, density-energy, and energy-energy correlation functions at $T = 0.13$ for different wavevectors. It is seen that these three different correlation functions have the same characteristics as discussed above, in agreement with the hydrodynamic predictions. It is also observed that the thermal diffusion process becomes more and more dominant in the low frequency limit as the length scale decreases. This is also the case for the Lennard-Jones liquid. Figure 6 (b) plots the Brillouin peak frequency, ω_{sound}, which according to the theory, Eq. (19), is linear with respect to wavevector. The wavevector-

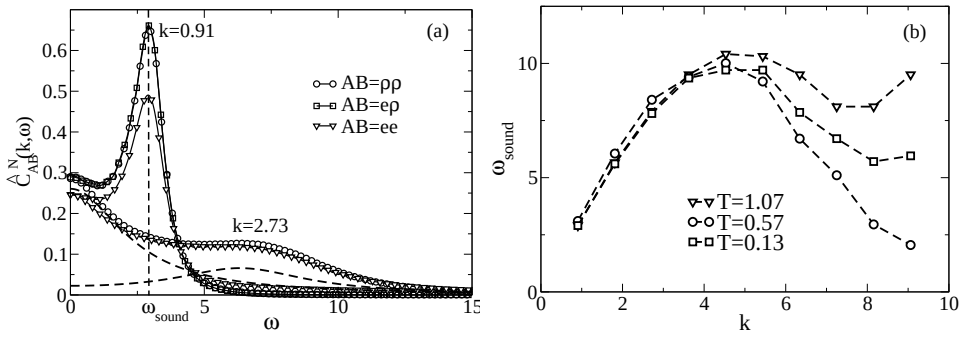

FIG. 6. (a) $\widehat{C}^N_{\rho\rho}, \widehat{C}^N_{e\rho}$, and $\widehat{C}^N_{ee}$ for different wavevectors. ω_{sound} is estimated from the lowest wavevector $k = 0.91$. (b) The dispersion relation. Lines serve as a guide to the eye.

dependent speed of sound features a maximum, which is also observed for simple liquids [19] like the Lennard-Jones system.

So far we have only considered collective dynamics as these are the predictions from hydrodynamics. As a final study of the wavevector-dependent dynamics, we investigate the single particle diffusivity. From the diffusion equation the incoherent scattering function (self-part of the intermediate scattering function), $F_s(\mathbf{k}, t)$, is in the small wavevector and frequency limits given by [19]

$$F_s(\mathbf{k}, t) = e^{-D_s k^2 t}\,, \tag{34}$$

where D_s is the self-diffusivity coefficient. In Fig. 7, data for the incoherent scattering function are shown for three different temperatures, $T = 0.13$, 0.36, and 1.07. The predictions from the theory, Eq. (34), are also shown as dashed lines, using the zero wavevector and zero frequency self-diffusion coefficients listed in Table I. The observations are identical to the transverse velocity relaxation: For high temperatures the theoretical prediction fails, whereas for low temperatures the agreement is excellent. It is important here to stress that the agreement at lower temperatures is likely related to the much slower relaxation time, and that the fast relaxation for high temperatures is not expected to be captured by the classical hydrodynamic theory as the low frequency limit is not reached.

V. SUMMARY AND CONCLUSIONS

In this paper the hydrodynamic relaxations of the original dissipative particle dynamics (o-DPD) model were investigated. First, the well-known results that the structure and

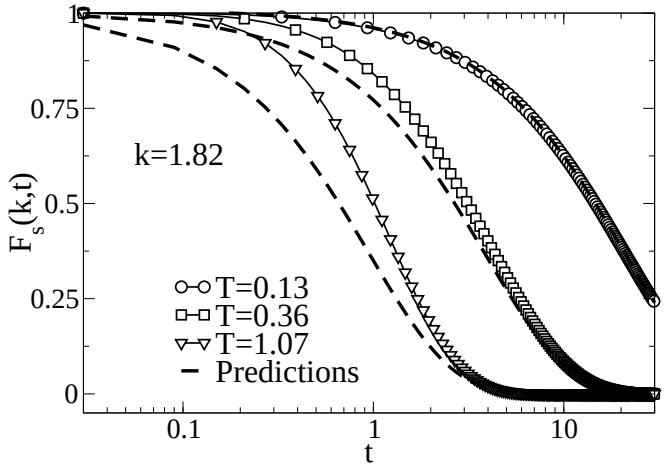

FIG. 7. The incoherent intermediate scattering function for different temperatures. The simulation data are compared with the predictions from the diffusion equation (dashed lines).

Schmidt number at high temperatures ($0.5 < T$) resemble those of a gas were recaptured. At the lowest temperature studied here, $T = 0.13$, the Schmidt number is approximately 50 and the fluid structure is observed to resemble that of a Lennard-Jones liquid. In the limit of zero wavevector and in the low temperature regime the shear modulus relaxation is Maxwellian to a good approximation; this cannot be concluded for higher temperatures, however. The Maxwell relaxation time increases with decreasing temperature as expected. However, the viscosity does not increase at the same rate, which results in a surprising decrease in the instantaneous shear modulus with decreasing temperature.

For nonzero wavevectors, the hydrodynamic prediction for the transverse velocity autocorrelation function is in very good agreement with simulation data in the low temperature regime, but fails for higher temperatures. This is in line with the fact that classical hydrodynamics fails for gasses. A qualitative investigation into the longitudinal dynamics was also carried out. For the gas-like regime the density longitudinal spectrum at low wavevectors is characterized by a single sharp Brillouin peak. This indicates that the longitudinal relaxation is dominated by propagating damped density waves. This mechanism is very different compared to a simple liquid, in which the thermal diffusion process dominates at low wavevector. In the low temperature range, the Rayleigh peak is more prominent; again this is a fingerprint of the more liquid-like state. The fact that classical hydrodynamics break down for higher temperatures is also observed for the self-part of the intermediate scattering function, that is, for the single particle dynamics.

In conclusion, the o-DPD model cannot act as a model for fluctuating hydrodynamics for higher temperatures. The exact temperature limit is not clear as this depends on the specific choice of free model parameters such as density, repulsion parameter, friction coefficient, and so forth. We recommend a Schmidt number well above unity for the model to have the correct hydrodynamic behavior.

VI. ACKNOWLEDGMENTS

Innovation Fund Denmark supported this work as a part of the ROSE project (no. 5160-00009B). MLG acknowledges support from the US Fulbright Program.

[1] P.J. Hoogerbrugge and J.M.V.A. Koelman. Simulatiing Microscopic Hydrodynamics Phenomena with Dissipative Particle Dynamics. *Europhys. Lett.*, 19:155, 1992.

[2] P. Español and P. Warren. Statistical Mechanics of Dissipative Particle Dynamics. *Europhys. Lett.*, 30:191, 1995.

[3] W. Kob and H.C. Andersen. Effect of solvent quality on the conformation and relaxation of polymers via dissipative particle dynamics. *J. Chem. Phys.*, 107:592, 1997.

[4] K.E. Novik and P.V. Coveney. Spinodal decomposition of off-critical quenches with a viscous phase using dissipative dynamics in two and three spatial dimensions. *Phys. Rev. E*, 61:435, 2000.

[5] A. Boromand, S. Jamali, and J.M. Maia. Viscosity measurement techniques in Dissipative Particle Dynamics. *Comp. Phys. Comm.*, 196:149, 2015.

[6] S.K. Ranjith, S. Vedantam, and B.S.V. Patnaik. Hydrodynamics of flow through microchannels with hydrophobic strips. *Microfl. Nanofl.*, 19:547, 2015.

[7] P. Español. Simu: Challenges in Molecular Simulations, Issue 4, Chap. III (2002).

[8] E. Moeendarbary, T.Y Ng, and M. Zangeneh. Dissipative Particle Dynamics: Introduction, methodology, and complex fluid application - a review. *Int. J. Appl. Mech.*, 1:737, 2009.

[9] R.D. Groot and P.B. Warren. Dissipative particle dynamics: Bridging the gap between atomistic and mesoscopic simulation. *J. Chem. Phys.*, 107:4423, 1997.

[10] P. Español and P. Warren. Perspective: Dissipative Particle Dynamics. *arXiv.org*, cs.SI, Dec. 2016.

[11] D. A. Mcquarrie. *Statistical Mechanics*. Harper and Row, New York, 1976.

[12] E.E. Keaveny, I.V. Pivkin, M. Maxey, and G.E. Karniadakis. A comparative study between dissipative particle dynamics and molecular dynamics for simple- and complex-geometry flows. *J. Chem. Phys.*, 123:104107, 2005.

[13] J. A. Backer, C. P. Lowe, H. C. J. Hoefsloot, and P. D. Iedema. Poiseuille flow to measure the viscosity of particle model fluids. *The Journal of Chemical Physics*, 122:154503, 2005.

[14] H. Reddy and J. Abraham. Dissipative-particle dynamics simulations of flow over a stationary sphere in compliant channels. *Physics of Fluids*, 21:053303, 2009.

[15] J.P. Boon and S. Yip. *Molecular Hydrodynamics*. Dover Publication, New York, 1991.

[16] L. Onsager. Reciprocal relations in irreversible processes. I. *Phys. Rev.*, 37:405, 1931.

[17] L.P. Kadanoff and P.C. Martin. Hydrodynamic Equations and Correlation Functions. *Ann. Phys.*, 24:419, 1963.

[18] W. E. Alley and B. J. Alder. Generalized transport coefficients for hard spheres. *Phys. Rev. A*, 27:3158, 1983.

[19] J. P. Hansen and I. R. McDonald. *Theory of Simple Liquids*. Academic Press, Amsterdam, 2006.

[20] J.S. Hansen, J.C. Dyre, P.J. Daivis, B.D. Todd, and H. Bruus. Continuum Nanofluidics. *Langmuir*, 31:13275, 2015.

[21] J.M.O. de Zárate and J.V. Sengers. *Hydrodynamic Fluctuations*. Elsevier, Amsterdam, 2006.

[22] E.J. Maginn, A.T. Bell, and D.N. Theodorou. Transport diffusivity of methane in silicalite from equilibrium and nonequilibrium simulations. *The Journal of Physical Chemistry*, 97(16):4173–4181, 1993.

[23] S. R. de Groot and P. Mazur. *Non-equilibrium Thermodynamics*. Dover Publications, 1984.

[24] J.H. Irving and J.G. Kirkwood. The statistical mechanical theory of transport processes. iv. the equations of hydrodynamics. *J. Chem. Phys.*, 18:817–829, 1950.

[25] J.E. Jones. On the Determination of Molecular Fields ii. from the Equation of State of a Gas. *Proc. R. Soc. Lond. A*, 106:463, 1924.

[26] D. Frenkel and B. Smit. *Understanding Molecular Simulation*. Academic Press, London, 1996.

[27] S. Nosé. A molecular dynamics method for simulation in the canonical ensemble. *Mol. Phys.*, 52:255–268, 1984.

[28] W. G. Hoover. Canonical dynamics: Equilibrium phase-space distributions. *Phys. Rev. A*, 31:1695–1697, 1985.

[29] J.D. Ferry. *Viscoelastic Properties of Polymers*. Wiley & Sons, Inc., New York, 1980.

[30] L. Bocquet and E. Charlaix. Nanofluidics, from bulk to interface. *Chem. Soc. Rev.*, 39:1073, 2010.

[31] J. S. Hansen, P. J. Daivis, K. P. Travis, and B. D. Todd. Parameterization of the nonlocal viscosity kernel for an atomic fluid. *Phys. Rev. E*, 76:041121, 2007.